

# Heat Generation by Irradiated Complex Composite Nanostructures

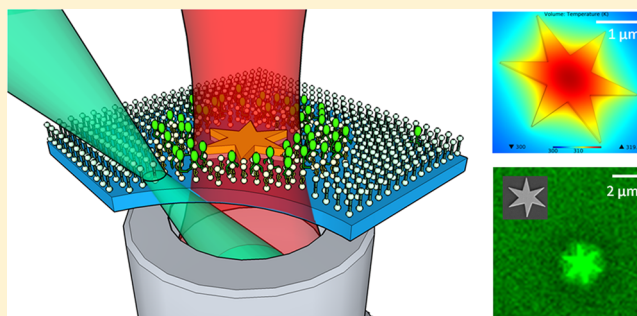
Haiyan Ma,<sup>†</sup> Pengfei Tian,<sup>†</sup> Josselin Pello,<sup>‡</sup> Poul Martin Bendix,<sup>†</sup> and Lene B. Oddershede<sup>\*,†</sup>

<sup>†</sup>Niels Bohr Institute, University of Copenhagen, Copenhagen, Denmark

<sup>‡</sup>COBRA Research Institute, Eindhoven University of Technology, Eindhoven, The Netherlands

**S** Supporting Information

**ABSTRACT:** Heating of irradiated metallic e-beam generated nanostructures was quantified through direct measurements paralleled by novel model-based numerical calculations. By comparing discs, triangles, and stars we showed how particle shape and composition determines the heating. Importantly, our results revealed that substantial heat is generated in the titanium adhesive layer between gold and glass. Even when the Ti layer is as thin as 2 nm it absorbs as much as a 30 nm Au layer and hence should not be ignored.



**KEYWORDS:** Plasmonics, nanoparticles, finite element method, e-beam lithography, heating, irradiation

Upon irradiation at the plasmon resonance of a metallic nanostructure, electromagnetic energy is absorbed and dissipated as heat into the surrounding media. Although metallic nanostructures of different compositions and sizes have been numerically investigated with the goal of controlling and understanding the heating, a gap still existed between theoretical predictions and experiments. The temperature of irradiated metallic nanostructures can easily reach hundreds of degrees Celsius,<sup>1</sup> thus enabling novel applications in chemical catalysis,<sup>2</sup> optofluidics,<sup>3</sup> drug delivery,<sup>4</sup> photothermal therapies,<sup>5</sup> or vapor generation.<sup>6</sup> There has been significant progress in modeling the thermo-plasmonic effect of nanostructures.<sup>7,8</sup> The discrete dipole approximation (DDA)<sup>9</sup> and the boundary element method (BEM)<sup>10,11</sup> have been extensively used to calculate plasmonic properties.<sup>12</sup> These methods are well suited for colloidal particles, whose geometries are relatively simple but still in need of further developments to analyze complex plasmonic devices. Several experimental assays were designed to measure the temperature increase on and around plasmonic devices.<sup>13–18</sup> However, most structures studied were relatively simple, as, for example, massive gold spheres, located in a uniform environment. This is in contrast to reality where much more complex nanostructures in inhomogeneous environments are often encountered. Here, we systematically quantify the temperature profiles of irradiated metallic composite structures: electron-beam printed discs, triangles, and stars of varying size. Our approach is both experimental using a novel method based on a lipid bilayer assay<sup>18,19</sup> and theoretical using a finite element numerical model (see Methods). We demonstrate that the titanium adhesive layer routinely used to improve the stability of gold structures fabricated on glass substrate has a dramatic thermal impact that has been somewhat overlooked in literature.

E-beam lithography is one of the most commonly used technologies to produce plasmonic structures such as nano-tweezers<sup>20,21</sup> or plasmonic absorbers.<sup>8,22</sup> The metallic nanostructures used here were prepared on a glass substrate via a standard e-beam lithography lift-off procedure (see Methods and Supporting Information Figure S1). All composite structures experimentally studied consisted of a 30 nm thick gold layer on top of a 20 nm titanium adhesive layer deposited on glass. The glass surface and deposited nanostructures were coated by a gel-phase lipid bilayer (details given in Methods). Phase sensitive lipophilic chromophores (DiOC<sub>18:2</sub>) up-concentrated in the melted regions around the irradiated nanostructures as schematically shown in Figure 1a. The extent of the melted region was quantified by confocal fluorescence imaging (Figure 1b), a rotational average of the intensity is shown in Figure 1c. The radius of the melted area,  $r_m$ , was determined as shown in Supporting Information Figure S2. As the phase transition is relatively sharp (Supporting Information Figure S3), the temperature at the boundary,  $T_m$ , is well-known. The temperature increase at  $r_m$ ,  $\Delta T(r_m) = T_m - T_b$  (where  $T_b$  is the temperature before irradiation) is of particular importance to deduce the temperature increase,  $\Delta T(r)$ , at a distance,  $r$ , far away from the irradiated structure<sup>19</sup>

$$\Delta T(r) = \frac{r_m}{r} \Delta T(r_m) \quad r \gg r_{st} \quad (1)$$

where  $r_{st}$  is the radius of the nanostructure.

Scanning electron microscope (SEM) images of the structures are shown in Figure 1d and schematically drawn in Figure 2a,b. The experimentally determined radii of their

**Received:** October 11, 2013

**Revised:** December 20, 2013

**Published:** January 6, 2014

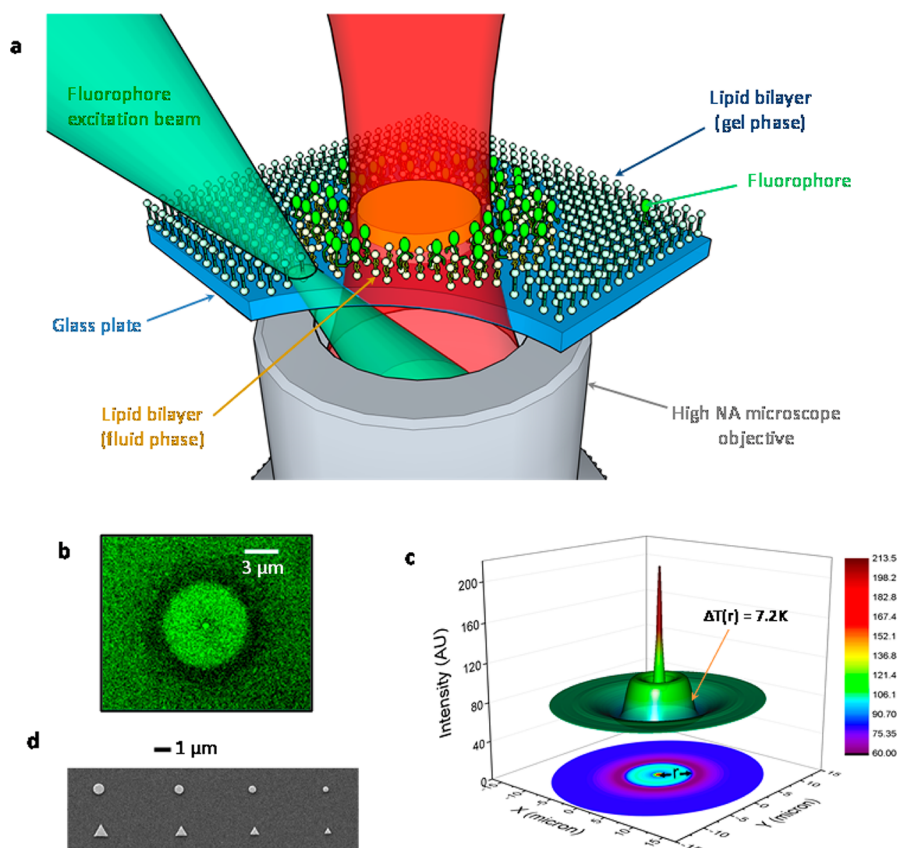


**Figure 1.** Experimental methodology. (a) Illustration of the setup (dimensions not to scale). A heating laser ( $\lambda = 1064$  nm, red) is focused onto an electron beam printed nanostructure. The metallic nanostructure absorbs light and dissipates heat into the surrounding lipid bilayer, where the lipid switches from gel phase into fluid phase. The lipid region is visualized by incorporating phase sensitive fluorophores (DiOC<sub>18:2</sub>) into the bilayer. (b) A typical image (denoted a melting fingerprint) of an irradiated circular disc ( $d = 500$  nm, thickness of lower titanium layer = 20 nm, thickness of upper gold layer = 30 nm). The partitioning of DiOC<sub>18:2</sub> into the fluid phase leaves behind a darker circular region in the nearby gel phase where the fluorophores are partially depleted. (c) A rotational average of the intensity of melting fingerprint shown in (b).  $r_m$  (red arrow) is the radial distance where the temperature rise  $\Delta T$  is equal to the difference between  $T_b$  and  $T_m$ . The color bar gives the intensity scale. (d) SEM images of the studied metallic discs and triangles, the surface area being constant in each column.

thermal fingerprints as a function of laser power are shown in Figure 2c,d. The laser power was kept below 4 mW to avoid heat induced reshaping.<sup>19</sup> For both triangles and discs, the measured thermal fingerprints increase linearly with the irradiating laser power.

The temperature far away from an irradiated nanodisc can be well predicted by eq 1; however, close to the surface eq 1 fails. To find the temperature profile of complex composite irradiated nanostructures we built a mathematical model and solved it by the finite element method (FEM). The generated heat per unit volume was described as<sup>22</sup>

$$Q_d(\mathbf{r}) = \frac{\omega \epsilon_0}{2} \text{Im}\{\epsilon_i(\mathbf{r}, \omega)\} |E(\mathbf{r}, \omega)|^2 \quad (2)$$

where  $\epsilon_i(\mathbf{r}, \omega)$  is the space- and wavelength-dependent relative permittivity,  $\epsilon_0$  is the permittivity of vacuum,  $\omega$  is the angular frequency of the laser light, and  $E(\mathbf{r}, \omega)$  is the electric field. To obtain the electric field of the nanostructure, we solved

$$\begin{aligned} \nabla \times \mu_r^{-1}(\nabla \times E(\mathbf{r}, \omega)) - K^2 \left( \epsilon_i(\mathbf{r}, \omega) - \frac{j\sigma}{\omega \epsilon_0} \right) E(\mathbf{r}, \omega) \\ = 0 \end{aligned} \quad (3)$$

Here,  $\mu_r$  is the relative permeability,  $K$  is the free space wavenumber, and  $\sigma$  the electrical conductivity. The static-state

temperature distribution  $T(\mathbf{r})$  was described by the Poisson equation. More model details are given in the Methods section.

The entire steady-state temperature profile for a disc and triangle under identical irradiation were calculated and plotted as insets in Figure 2a,b, respectively. The slightly asymmetric triangle temperature profile relates to the shape of the triangle. If the disc is treated as solid gold and the glass interface ignored, the discrepancy between the values returned by the full FEM and eq 1 is 15–30% (see also Supporting Information Figure S4). We extracted  $r_m$  from the simulations; these are shown in Figure 2c,d (with hollow circles and triangles, respectively). There is an excellent agreement between experimental (solid symbols) and theoretical results. In contrast to measurements on colloidal gold,<sup>19</sup> the experimentally obtained  $r_m$  does not lead to the surface temperature of the composite structures because the thermal conductivity of glass and the presence of Ti need to be taken into account due to the large contact areas. Furthermore, the interfacial thermoresistance<sup>23,24</sup> at the different interfaces dramatically influences the internal thermal diffusion of this sandwiched geometry.

By including both the interfacial coefficients for thermoresistance between the materials and the heat drain effect of the glass substrate, we deduced the surface temperature of the nanostructures. Figure 2e,f shows the simulated surface temperatures of discs and triangles as a function of laser

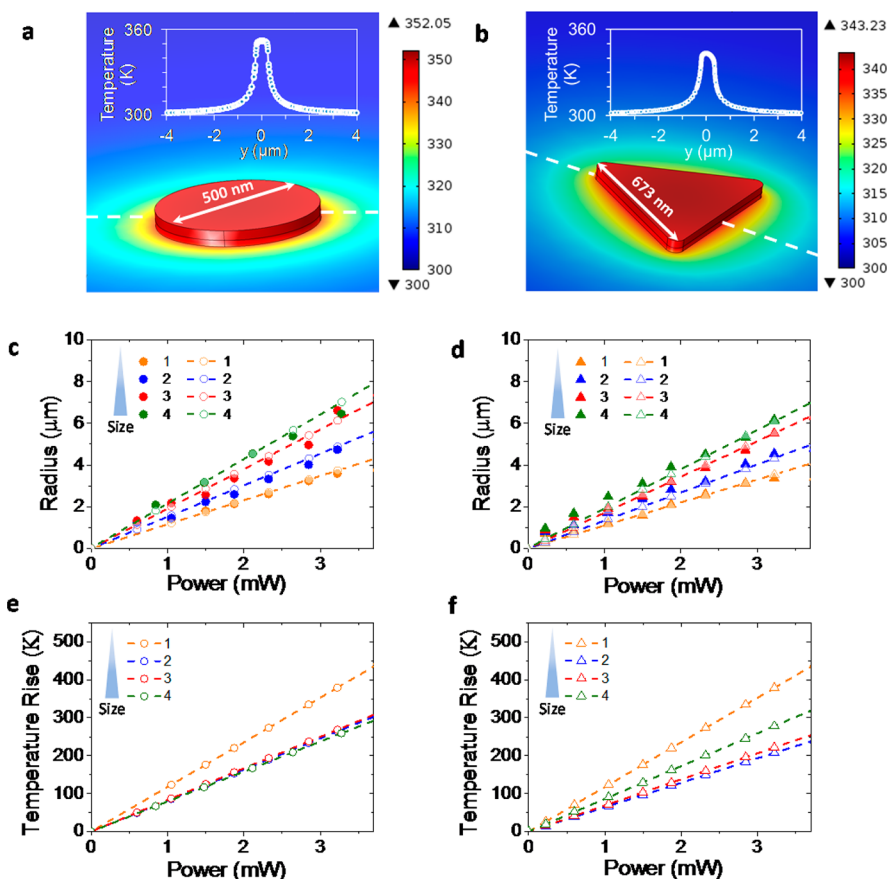


**Figure 2.** Steady-state temperature increase of irradiated discs and triangles composed of Ti and Au. (a,b) Temperature increase of a disc (a) with diameter = 500 nm and a triangle (b) with identical volume and side length = 673 nm irradiated by a laser with Gaussian intensity profile ( $\sigma = 0.7 \mu\text{m}$ , laser power  $P_0 = 0.6 \text{ mW}$ ). Background temperature: 300 K. The insets show the temperature profile along the white dashed lines in (a,b). (c,d) Quantification of the measured (solid symbols) and simulated (hollow symbols, dashed lines) radii of the melted fingerprints for irradiated (c) discs and (d) triangles as function of laser power. The cross sectional areas (and volumes) of discs and triangles denoted with the same number are identical, these cross sectional areas are 1:  $\pi \times 10^4 \text{ nm}^2$ , 2:  $4\pi \times 10^4 \text{ nm}^2$ , 3:  $6.25\pi \times 10^4 \text{ nm}^2$ , and 4:  $9\pi \times 10^4 \text{ nm}^2$ . The radii of discs 1, 2, 3, and 4 are 100, 200, 250, and 300 nm, respectively. The side lengths of triangles 1, 2, 3, and 4 are 269, 538, 673, and 808 nm, respectively. (e,f) Calculated temperature increases on discs 1–4 (e) and triangles 1–4 (f) as a function of laser power.

power. For both shapes, the smallest nanostructures have the highest surface temperature elevation. This is reasonable because the surface plasmon resonance of the smallest structures nearly coincides with the wavelength of the heating laser, whereas the absorption of the larger structures are significantly lower and nearly identical (see Supporting Information Figure S5). The heating rates for the smallest discs and triangles are nearly identical (disc, 117.6 K/mW; triangle, 117.5 K/mW), whereas the heating rates for the larger structures are somewhat smaller ( $\sim 80\text{--}90 \text{ K/mW}$ ). Hence, under NIR irradiation a rounded structure is equally photothermally efficient as a triangle with sharp ends.<sup>7</sup>

In nanofabrication, titanium is widely used to improve the adhesion of gold onto glass substrates. The thickness of the Ti adhesive layer differs greatly in nanostructures fabricated for distinctive applications in different research groups.<sup>25–28</sup> The change of plasmonic properties, for example, the broadening and red shift of the plasmon resonance peak, induced by the Ti adhesive layer has been thoroughly studied for split-ring resonators<sup>27,28</sup> and nanorods.<sup>28</sup> However, the influence of the thickness of the adhesive Ti layer on the overall thermal properties of metallic nanostructures was not previously reported.

To investigate the influence of the Ti adhesive layer on the thermal properties of composite nanostructures, we calculated the absorbed heat power in the Au layer and in the Ti layer of composite Au/Ti discs and triangles irradiated by a laser intensity of  $1 \text{ mW}/\mu\text{m}^2$ . The thickness of the gold layer was kept constant (30 nm), whereas the thickness of the Ti layer was varied from 0 to 30 nm (0, 2, 5, 10, 20, and 30 nm). As the thickness of the Ti layer increases, the absorbed power increases in the Ti layer and decreases in the Au layer for both shapes as shown in Figure 3. In the experiments (sketched in Figure 1), an inverted microscope was used, hence the Ti layer was irradiated prior to the Au layer and the Ti layer had a “shielding effect”. The plasmon resonance peak of the composite structures gradually shifts to a longer wavelength as the thickness of the Ti layer increases (as shown in Supporting Information Figure S6) in accordance with the observations from nanorods and split-ring resonators.<sup>26–28</sup> Even when the Ti layer is as thin as 1 nm, plasmon damping effects can still be drastic.<sup>26</sup> Apart from the plasmon damping effect induced by Ti or Cr adhesive layers,<sup>29</sup> the absorptive nature of Ti also results in a significant thermal effect. As shown in Figure 3, the absorbed power in the Ti layer can reach a high level in both discs and triangles, even a 2 nm thin Ti layer underneath 30 nm Au absorbs 45.7% and 42.3% for the disc

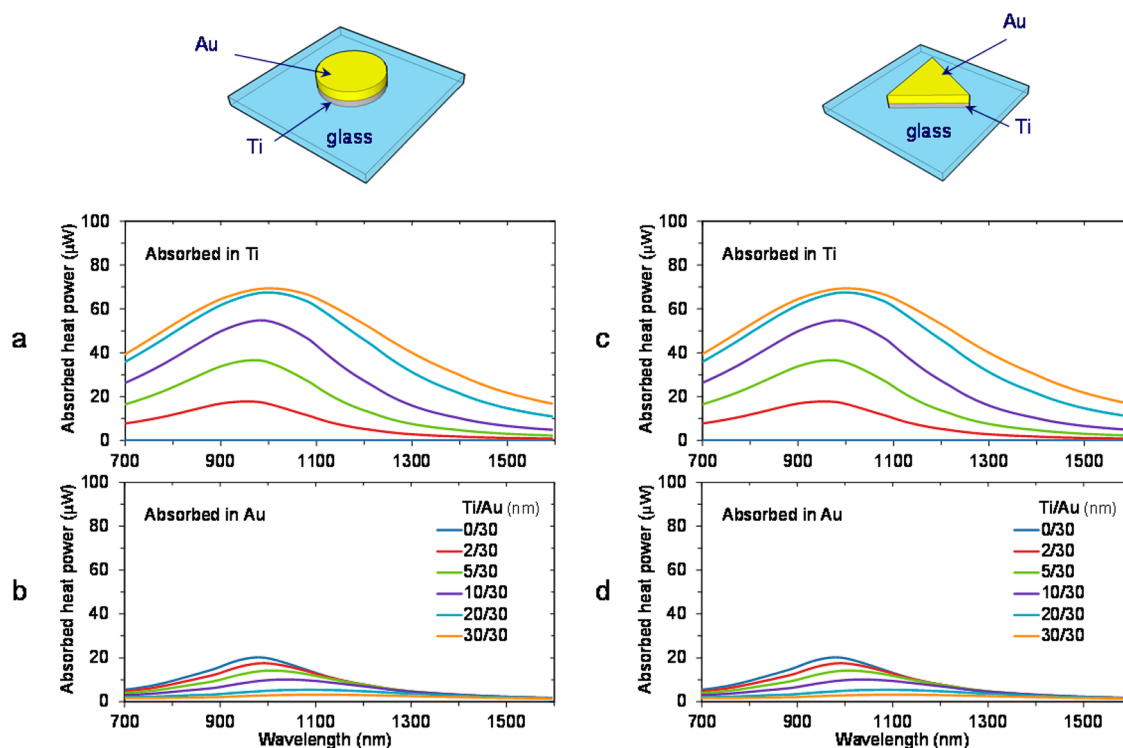


**Figure 3.** Comparison of the heat generation in the titanium adhesive layer (thickness varied from 0 to 30 nm) and in the gold layer (fixed thickness = 30 nm) in composite discs and triangles of identical volume. (a,b) Calculated absorbed heat power in the Ti layer (a) and the Au layer (b), as a function of wavelength in a composite disc (diameter = 200 nm), when setting the Ti layer thickness to 0, 2, 5, 10, 20, and 30 nm, successively. (c,d) Calculated absorbed heat power in the Ti layer (c) and the Au layer (d), as a function of wavelength in a composite triangle (side length = 269 nm) of identical volume as the disc, when setting the Ti layer thickness to 0, 2, 5, 10, 20, and 30 nm, successively. The irradiation laser intensity is 1 mW/ $\mu\text{m}^2$ .

and triangle, respectively, of the total absorbed heat power at 1064 nm. If the Ti layer becomes 20 nm thick, the heat power absorbed in the Ti slab is 92.4% (for the disc) and 90.7% (for the triangle) of the total absorbed power. These results show that the thermal contribution of the Ti layer cannot be neglected even for thin Ti layers, when a composite structure is irradiated from the side of the Ti layer. The calculated average temperature rise on the composite discs and triangles as a function of the Ti adhesive layer thickness is plotted in Supporting Information Figure S7. The structures were irradiated by a Gaussian intensity profile with  $\sigma = 0.7 \mu\text{m}$  and a total power of 0.6 mW. Without the Ti adhesive layer, the average temperature increase on the Au disc and triangle is 16.5 °C and 27 °C, respectively (Supporting Information Figure S7). By adding a 2 nm Ti adhesive layer, the average temperature rises up to 29.2 °C for the disc and 38.8 °C for the triangle, which is clearly non-negligible. Chromium is also often used as an adhesive layer for Au structures, however, as chromium absorbs even more than Ti,<sup>30</sup> an adhesive chromium layer will influence the thermo-plasmonic properties even more than a Ti layer does.

To experimentally verify the influence of the adhesive Ti layer on heat generation, we compare the theoretical findings to experimentally measured heating properties of an Au/Ti composite disc and a pure Ti disc (see sketches in Figure 4a). In Figure 4b, we show the calculated absorption cross section of each structure as a function of the irradiation laser wavelength. The overall absorption cross section of the pure titanium disc is higher than that of the composite disc over the whole spectrum, including at the wavelength of the heating

laser ( $\lambda = 1064 \text{ nm}$ ). Because the thermal conductivity of Ti is  $\sim 46$  times<sup>31,32</sup> smaller than that of Au, the titanium disc is indeed expected to cause a much greater temperature elevation. We quantified the sizes of the melted fingerprints at various laser powers (circles in Figure 4c) obtained in experiments, which agree well with the size obtained from the FEM simulations (full lines in Figure 4c). The corresponding temperature increases are plotted in the inset of Figure 4c. Clearly, a pure titanium disc generates more heat than a composite Ti/Au disc, regardless of the excitation power. These observations verify the fact that Ti is an efficient photothermal converter in the NIR region. Together with the results demonstrated in Figure 3, we believe that cautious steps have to be taken before neglecting the thermal contribution of Ti under heat sensitive conditions. Furthermore, alternative adhesion materials<sup>26</sup> should be considered to replace Ti (or Cr) to minimize undesirable thermal effects.

In the nascent field of nanoplasmonics, more exotic nanostructures are often designed to achieve extreme and local field enhancements. Structures having sharp edges or gaps are particularly efficient in concentrating light at the nanoscale. To show the robustness of our experimental and numerical approaches when applied to such structures with more complicated shapes we examined theoretically and experimentally a star and a dimer (i.e., a pair of aligned nanorods). The sharp tips of stars and the gap between two rods are commonly used for localized plasmon enhancement;<sup>33–35</sup> however, probably due to the complexity of the structures their associated thermo-plasmonics properties were never quantified. We created a six-branched star ( $d = 2880 \text{ nm}$ ) and two

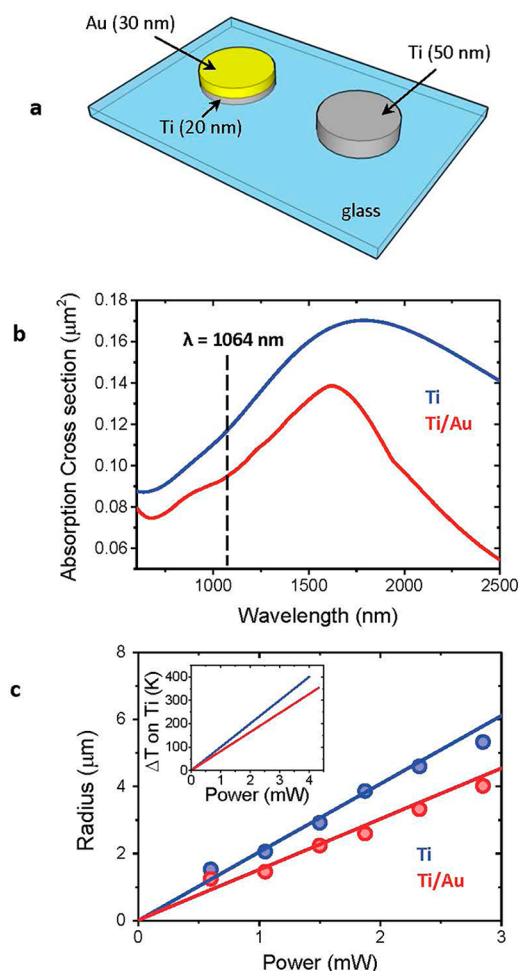


**Figure 4.** Comparison between the heat generation of a composite disc (30 nm Au on top of 20 nm Ti,  $d = 400$  nm) and a pure Ti disc (thickness 50 nm) of identical volumes. (a) Sketches of the two structures under comparison. (b) Calculated absorption cross section of the pure Ti disc (blue) and the composite Ti/Au disc (red) as a function of wavelength. The dashed line shows the wavelength of the heating laser. (c) Experimentally measured radii of composite Au/Ti discs (red circles) and pure Ti discs (blue circles), the full line shows the calculated size of the melted fingerprints. The inset shows the corresponding temperature increase (Au/Ti, red; pure Ti, blue). In all experiments, the structures were illuminated by a Gaussian intensity profile with  $\sigma = 0.7$   $\mu\text{m}$ .

nanorods (each  $150$  nm  $\times$   $500$  nm) aligned end-to-end with a gap of  $500$  nm by e-beam lithography, SEM images of these structures are shown as insets in Figure 5e,f. The modeled structures used for the FEM analysis are shown in Figure 5a,b. The isotherms of the simulated temperature profiles around a star (Figure 5c) and a dimer (Figure 5d) are hexagonal and elliptical, respectively; well matched, both qualitatively and quantitatively, by the experimentally measured fingerprints, which are shown in Figure 5e,f.

On the basis of direct experimental measurements and our novel numerical model, we quantified and compared the thermal response of two types of nanostructures (discs and triangles) with identical volume and under identical laser irradiation. Both shapes generate a significant temperature rise, while the smallest structures that are resonant with the irradiating laser achieve the highest temperatures, see Figure

2e,f. Interestingly, despite their sharp tips the triangles do not heat more than discs.

We also investigated the photothermal effect of titanium, which is routinely used as an adhesive layer in e-beam generated gold nanostructures. Importantly, we find that titanium has a huge effect (see Figure 3) and that pure titanium discs generate an even larger temperature increase around the structure than composite gold–titanium structures of identical shape and volume. This finding can provide guidance for future design of plasmonic devices, especially for biorelated applications such as photothermal treatments where titanium has the advantage of being biocompatible and cost efficient.

A comparison of all the structures investigated, discs, triangles, stars, and dimers, shows that even though the local isotherms resemble the shape of the irradiated nanostructure (as shown in Figure 5c–f), the overall melted radii,  $r_m$ , and the surface temperatures are actually quite comparable. This is visualized in Figure 6, which shows  $r_m$  as function of the cross sectional area for all investigated structures, the irradiating laser power was kept constant during this experiment. The melted radius around all sizes of discs, triangles, and stars follow the same linear increase with cross sectional area of the irradiated structure. The dimer falls below this linear increase, probably because of experimental difficulties with centering the laser beam exactly at the gap. Using the FEM we calculated the corresponding temperature increases at the surface of the particles; these are shown in the inset of Figure 6. The temperature increase at the surface of all irradiated structures appears to reach a constant value of  $140$ – $150$  K, except for the smallest disc and triangle, whose absorption is resonant with the irradiating laser (see Supporting Information Figure S5). As expected, the dimer falls below this trend.

In conclusion, our experimental and numerical methodologies allow for determination of temperature profiles around irradiated nanostructures of any shape, size, and composition. This is of crucial importance for development of several applications, for example, efficient nanoears<sup>35</sup> or for thermophoresis.<sup>36</sup> Our finding of significant heating contribution by the titanium slab, even when it is as thin as  $2$  nm, will impact future design of plasmonic devices. Furthermore, since titanium is extremely biocompatible, this discovery will optimize material selection for photothermal therapies.

**Methods.** The metallic nanostructures studied in this work were fabricated on a glass coverslip using the e-beam lithography (EBL) lift-off process described in Supporting Information Figure S1. Prior to fabrication, a 1 inch diameter glass coverslip was sonicated in deionized water for 2 min and submitted to an  $\text{O}_2$  plasma treatment (300 W, 10 min) to remove particles and dirt from the surface. Polymethylmethacrylate (PMMA 950K A4) electron-sensitive resist was then spun on the glass coverslip and a  $12$  nm thick layer of gold evaporated on top to prevent charging effects during EBL (cf. Supporting Information Figure S1(i)). In the next step, the areas of the future metallic nanostructures were exposed in an EBL machine using a voltage of  $20$  kV. After the exposure, the gold layer was removed in  $\text{KI}/\text{I}_2$  and the exposed PMMA developed in a mixture of methyl isobutyl ketone (MIBK) and isopropanol (IPA), as shown in Supporting Information Figure S1(ii). An evaporator was then used to deposit titanium ( $50$  nm) or titanium/gold ( $20$  nm/ $30$  nm) on the surface of the sample (see Supporting Information Figure S1(iii)). Finally, the sample was put in acetone for 30 min to dissolve the remaining

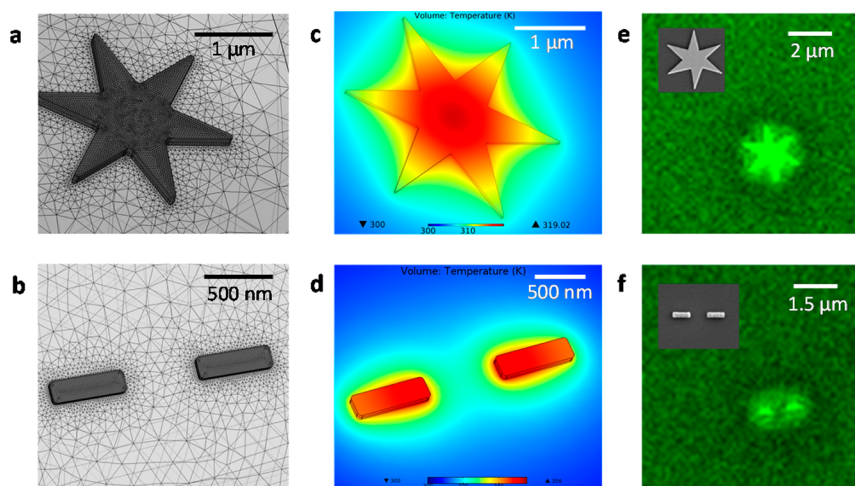


**Figure 5.** Comparison between the simulated and measured temperature profiles around exotic composite structures (with 30 nm Au on top of 20 nm Ti). The laser power on the star was 0.22 mW, on the dimer 1.9 mW, background temperature 300 K. (a,b) Finite element meshing scheme of simulated six-branch star (a) and dimer (b) on glass substrates with the minimum element width equal to 10 nm, generated by COMSOL. (c,d) Simulated temperature distributions around a star (c) and a dimer (d) under laser irradiation. The average surface temperature of the star reached 315 K, of the dimer 348 K. (e,f) Measured melting fingerprints of a star (e) and a dimer (f). For the star, the measured radius of the melted region is  $r_m = 1.44 \mu\text{m}$ , the simulated one  $r_m = 1.32 \mu\text{m}$ . For the dimer, the elliptical melted region is  $1.584 \mu\text{m} \times 1.08 \mu\text{m}$ , the simulated region  $1.587 \mu\text{m} \times 1.33 \mu\text{m}$ . The insets of (e,f) show SEM images of the star and dimer before the beginning of the experiments.

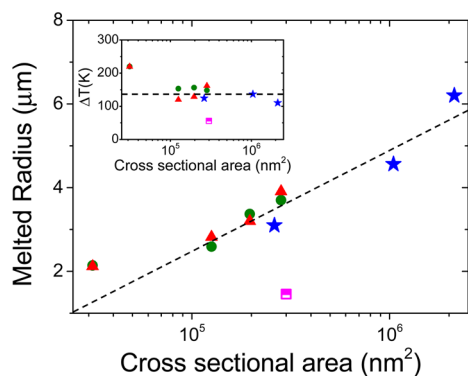


**Figure 6.** Comparison of the plasmonic properties of nanostars, discs, triangles, and dimers. The irradiating laser power was kept constant at 1.9 mW during this entire experiment.  $r_m$  is plotted versus the cross sectional area for irradiated stars (blue), discs (green), triangles (red), and dimers (pink). The dashed line shows a linear relation between  $r_m$  and cross sectional area, a relationship obeyed by all structures (apart from the dimer). The inset shows the temperature increase at the surface of the irradiated structures as a function of the cross sectional area calculated by the FEM. The horizontal line shows the temperature increase of the majority of the irradiated structures; only the smallest discs and triangles (resonant with the laser) have temperature increases significantly above this line.

PMMA and lift-off the metal stack from the regions where it was not needed (cf. Supporting Information Figure S1(iv)). After rinsing the sample in IPA, the structures were ready for use.

The lipid bilayer was composed of 1,2-dipentadecanoyl-sn-glycero-3-phosphocholine (DC<sub>15</sub>PC, Avanti Polar Lipids) and 0.75 mol % 3,3'-dilinoleyloxycarbocyanine perchlorate (DiOC<sub>18:2</sub>) fluorophores. This lipid mixture has a well-defined phase transition temperature (Supporting Information Figure S2)  $T_m \sim 33.8 \text{ }^\circ\text{C}$  above which the lipid molecules change from an organized gel phase into a more disordered fluid phase. The mixture of lipids and fluorophores was first dissolved in chloroform and then evaporated onto a glass vial under

nitrogen flow to create a thin film. The thin film was dried in vacuum for 2 h followed by hydration with PBS buffer (pH = 7.4, 150 mM NaCl) at 37 °C. To form small unilamellar vesicles, we extruded the hydrated lipid mass through polycarbonate filters with 50 nm pore size at  $T = 37 \text{ }^\circ\text{C}$ . The glass substrate on which metallic nanostructures were printed had undergone 5 min sonic bath to remove excessive particles on the surface prior to 10 min thorough O<sub>2</sub> plasma cleaning (Harrick Plasma). The clean and highly hydrophilic glass substrate was then used to support the lipid bilayer sensing assay. Finally, 200  $\mu\text{L}$  of extruded vesicles were flushed into a perfusion chamber and allowed to fuse to the glass substrate. It was important that the incubation temperature was higher than the gel-to-fluid phase transition temperature of  $T_m = 33.8 \text{ }^\circ\text{C}$ . Excess lipid vesicles were thoroughly washed out 15 times by vigorous pipetting using deionized water with the surface and fluid held at  $T \sim 40 \text{ }^\circ\text{C}$ . The final experiments were conducted at 26.6 °C in deionized water. The fluorophores were excited at 488 nm (green scanning beam in Figure 1a) and imaged through a high NA microscope objective in the spectral range of 500–530 nm with a Leica SP5 confocal microscope. At the same time, a heating laser (Spectra Physics J201-BL-106C, red beam in Figure 1a) with a beam radius of 0.7  $\mu\text{m}$  on the plane of the lipid bilayer was used to irradiate the metallic nanostructure and induce significant temperature elevation through photothermal conversion. During experiments, the background temperature ( $T_b$ ) of the sample was kept at 26.6 °C (below the phase transition temperature ( $T_m = 33.8 \text{ }^\circ\text{C}$ ) of the lipid bilayer, Supporting Information Figure S2), thus keeping the lipid bilayer in an organized gel phase. Once the heating laser was turned on and the nanostructure started to dissipate heat into the surrounding media, the organization of lipids contained in the area where the temperature exceeded the phase transition temperature ( $T > T_m$ ), switched to the more disorganized fluid phase. Subsequently, the fluorescent marker, DiOC<sub>18:2</sub>, which had unsaturated fatty acid tails and therefore energetically preferred to mix with disordered phases, diffused toward the melted bilayer region.

The spot size of the focused laser beam in the bilayer plane was measured by using the laser to bleach an area on an Alexa fluorophore labeled bovine serum albumin (BSA) layer.<sup>37</sup> The bleached profile matched the Gaussian intensity profile of the laser and a standard deviation of  $\sigma = 0.7 \mu\text{m}$  was found using a laser power of  $P_0 = 0.6 \text{ mW}$ .

The plasmonic model was solved using the FEM. The negative permittivities of gold and titanium give rise to resistive heat generation upon laser irradiation. The generated heat power per unit volume  $Q_d$  is described as  $Q_d(\mathbf{r}) = (\omega\varepsilon_0)/(2)\text{Im}\{\varepsilon_r(\mathbf{r},\omega)\}\{E(\mathbf{r},\omega)\}^2$ , where  $\varepsilon_r(\mathbf{r},\omega)$  is the space- and wavelength-dependent relative permittivity;  $\varepsilon_0$  is the permittivity of vacuum;  $\omega$  is the angular frequency of the laser; and  $E(\mathbf{r},\omega)$  is the electric field. In order to obtain the electric field of the nanostructure, we numerically solved the equation  $\nabla \times \mu_r^{-1}(\nabla \times E(\mathbf{r},\omega)) - K^2[\varepsilon_r(\mathbf{r},\omega) - (j\sigma/\omega\varepsilon_0)]E(\mathbf{r},\omega) = 0$  in FEM Multiphysics (COMSOL), where  $\mu_r$  is the relative permeability,  $K$  is the free space wavenumber, and  $\sigma$  is the electrical conductivity. Taking into account the Gaussian intensity distribution of the incoming laser irradiation, we deduct the average heat power density of a nanostructure with a volume  $V$  and describe it as  $[(2P_0)/(\pi\omega_z^2)][(\int Q_d(\mathbf{r})d\mathbf{r})/(IV)]e^{-2r_z^2/\omega_z^2}$ , where  $P_0$  is the laser power incident on the sample chamber,  $\omega_z$  is the beam radius in the plane of the lipid bilayer,  $I$  is the intensity of the incoming plane wave, and  $r_z$  is the distance from each point to the center of the nanostructure in the lipid bilayer plane. In the simulation, the nanostructures are confined in the center of a spherical domain (with a radius of  $2 \mu\text{m}$ ) with an upper aqueous domain and a lower glass domain. A 500 nm thick perfectly matched layer is also employed at the boundary of this spherical domain to minimize undesirable backscattering of the electromagnetic wave from the artificial boundary. Finally, the optical constants of gold and titanium were obtained from refs 38 and 39.

To solve the heat transfer model with the FEM, the steady-state temperature distribution  $T(\mathbf{r})$  was described by the Poisson equation  $\nabla \cdot [\kappa(\mathbf{r})\nabla T(\mathbf{r})] = -Q_s(\mathbf{r})$ , where  $\kappa(\mathbf{r})$  is the position-dependent thermal conductivity and  $Q_s(\mathbf{r})$  is the heat power density obtained by solving the plasmonic model. Two pieces of information are essential to solve the model. First, as the thickness of the nanofilm approaches the mean free path of the heat carrier, strong boundary scattering effects arise, consequently the thermal conductivity dramatically decreases. The thermal conductivities of a 30 nm thick gold film and a 20 nm thick titanium film in our model are set to  $91.6 \text{ W}/(\text{m}\cdot\text{K})$  and  $1.3 \text{ W}/(\text{m}\cdot\text{K})$ , respectively.<sup>31,32</sup> Second, for a multilayer thin film geometry the effect of finite thermal boundary conductance (TBC) caused by the discontinuity between different materials critically affects the heat transport within the nanostructure in the plane perpendicular to the material interfaces.<sup>24</sup> Such an effect results in a dramatic temperature gap between the interior boundaries (titanium–gold and titanium–silica). Experiments have shed light on the TBC of both metal–metal interface and metal–silica interface.<sup>23,40,41</sup> Inspired by ref 22 we incorporated this effect into our numerical model by inserting a virtual thin layer to restore the real temperature jump at the interface. The thermal conductivity  $k_c$  and thickness  $d$  of this virtual layer follow:  $f = (k_c/d)(T_A - T_B)$ , where  $f$  and  $T_A - T_B$  are the vertical heat flux and temperature difference of the materials A and B at the interface, respectively. Following this equation, the thin fictitious layer could mimic the discontinuous temperature

because of TBC at the interface of materials A and B.<sup>22</sup> The model was solved by the FEM taking into account the geometry of the structure. Infinite elements were utilized to simulate the unbounded background. The number of iterations used to solve the model was set to gain a relative tolerance better than  $10^{-6}$  in terms of the temperature. In order to verify that our experiments were carried out in thermal equilibrium, we calculated the dynamic temperature increase process using the equation  $C_s(\mathbf{r})\rho(\mathbf{r})[(\partial T(\mathbf{r}))/\partial t] + \nabla \cdot [\kappa(\mathbf{r})\nabla T(\mathbf{r})] = -Q_s(\mathbf{r})$ , where  $t$  is time and  $C_s(\mathbf{r})$  and  $\rho(\mathbf{r})$  are the position-dependent specific heat capacity and the material density, respectively.

## ■ ASSOCIATED CONTENT

### Supporting Information

Additional figures and reference. This material is available free of charge via the Internet at <http://pubs.acs.org>.

## ■ AUTHOR INFORMATION

### Corresponding Author

\*E-mail: [oddershede@nbi.dk](mailto:oddershede@nbi.dk). Phone: +45 35325287.

### Notes

The authors declare no competing financial interest.

## ■ ACKNOWLEDGMENTS

We thank S. Landa and K. Zecchi for assistance with the calorimetric measurements and X. Chen and H. Shen for fruitful discussions. We acknowledge financial support from a Niels Bohr Scholarship, the Villum Kann Rasmussen Foundation, the Lundbeck Foundation, and a University of Copenhagen Excellence grant.

## ■ REFERENCES

- Baffou, G.; Quidant, R. Thermo-plasmonics: using metallic nanostructures as nano-sources of heat. *Laser Photonics Rev.* **2013**, *7*, 171–187.
- Christopher, P.; Xin, H.; Linic, S. Visible-light-enhanced catalytic oxidation reactions on plasmonic silver nanostructures. *Nature Chem.* **2011**, *3*, 467–72.
- Thamdrup, L. H.; Larsen, N. B.; Kristensen, A. Light-Induced Local Heating for Thermophoretic Manipulation of DNA in Polymer Micro- and Nanochannels. *Nano Lett.* **2010**, *10*, 826–32.
- Huschka, R.; et al. Gene Silencing by Gold Nanoshell-Mediated Delivery and Laser-Triggered Release of Antisense Oligonucleotide and siRNA. *ACS Nano* **2012**, *6*, 7681–91.
- Huang, X.; El-Sayed, I. H.; Qian, W.; El-Sayed, M. A. Cancer Cell Imaging and Photothermal Therapy in the near-Infrared Region by Using Gold Nanorods. *J. Am. Chem. Soc.* **2006**, *128*, 2115–20.
- Neumann, O.; et al. Solar Vapor Generation Enabled by Nanoparticles. *ACS Nano* **2013**, *7*, 42–9.
- Baffou, G.; Quidant, R.; Girard, C. Heat generation in plasmonic nanostructures: Influence of morphology. *Appl. Phys. Lett.* **2009**, *94*, 153109.
- Coppens, Z. J.; Li, W.; Walker, D. G.; Valentine, J. G. Probing and Controlling Photothermal Heat Generation in Plasmonic Nanostructures. *Nano Lett.* **2013**, *13*, 1023–8.
- Yurkin, M. A.; Hoekstra, A. G. The discrete-dipole-approximation code ADDA: Capabilities and known limitations. *J. Quant. Spectrosc. Radiat. Transfer* **2011**, *112*, 2234–2247.
- García de Abajo, F.; Howie, A. Retarded field calculation of electron energy loss in inhomogeneous dielectrics. *Phys. Rev. B* **2002**, *65*, 115418.
- Hohenester, U.; Trügler, A. MNPBEM – A Matlab toolbox for the simulation of plasmonic nanoparticles. *Comput. Phys. Commun.* **2012**, *183*, 370–381.

- (12) Baffou, G.; Quidant, R.; Girard, C. Thermoplasmonics modeling: A Green's function approach. *Phys. Rev. B* **2010**, *82*, 165424.
- (13) Baffou, G.; Kreuzer, M. P.; Kulzer, F.; Quidant, R. Temperature mapping near plasmonic nanostructures using fluorescence polarization anisotropy. *Opt. Express* **2009**, *17*, 3291–3298.
- (14) Carlson, M. T.; Khan, A.; Richardson, H. H. Local temperature determination of optically excited nanoparticles and nanodots. *Nano Lett.* **2011**, *11*, 1061–9.
- (15) Boyer, D.; Tamarat, P.; Maali, A.; Lounis, B.; Orrit, M. Photothermal imaging of nanometer-sized metal particles among scatterers. *Science* **2002**, *297*, 1160–3.
- (16) Ruijgrok, P. V.; Verhart, N. R.; Zijlstra, P.; Tchebotareva, A. L.; Orrit, M. Brownian Fluctuations and Heating of an Optically Aligned Gold Nanorod. *Phys. Rev. Lett.* **2011**, *107*, 037401.
- (17) Baffou, G.; et al. Thermal Imaging of Nanostructures by Quantitative Optical Phase Analysis. *ACS Nano* **2012**, *6*, 2452–8.
- (18) Bendix, P. M.; Reihani, S. N.; Oddershede, L. B. Direct Measurements of Heating by Electromagnetically Trapped Gold Nanoparticles on Supported Lipid Bilayers. *ACS Nano* **2010**, *4*, 2256–62.
- (19) Ma, H.; Bendix, P. M.; Oddershede, L. B. Large-Scale Orientation Dependent Heating from a Single Irradiated Gold Nanorod. *Nano Lett.* **2012**, *12*, 3954–60.
- (20) Juan, M. L.; Righini, M.; Quidant, R. Plasmon nano-optical tweezers. *Nat. Photonics* **2011**, *5*, 349–356.
- (21) Wang, K.; Schonbrun, E.; Steinvurzel, P.; Crozier, K. B. Trapping and rotating nanoparticles using a plasmonic nano-tweezer with an integrated heat sink. *Nat. Commun.* **2011**, *2*, 469.
- (22) Chen, X.; Chen, Y.; Yan, M.; Qiu, M. Nanosecond Photothermal Effects in Plasmonic Nanostructures. *ACS Nano* **2012**, *6*, 2550–7.
- (23) Chien, H.-C.; Yao, D.-J.; Hsu, C.-T. Measurement and evaluation of the interfacial thermal resistance between a metal and a dielectric. *Appl. Phys. Lett.* **2008**, *93*, 231910.
- (24) Swartz, E.; Pohl, R. Thermal boundary resistance. *Rev. Mod. Phys.* **1989**, *61*, 605–668.
- (25) Anika Kinkhabwala, Z. Y.; Fan, S.; Avlasevich, Y.; Klaus Mullen; Moerner, W. E. Large single-molecule fluorescence enhancements produced by a bowtie nanoantenna. *Nat. Photonics* **2009**, *3*, 654–657.
- (26) Habteyes, T. G.; et al. Metallic Adhesion Layer Induced Plasmon Damping and Molecular Linker As a Nondamping Alternative. *ACS Nano* **2012**, *6*, 5702–9.
- (27) Jeppesen, C.; Mortensen, N. A.; Kristensen, A. The effect of Ti and ITO adhesion layers on gold split-ring resonators. *Appl. Phys. Lett.* **2010**, *97*, 263103.
- (28) Lahiri, B.; Dylewicz, R.; De La Rue, R. M.; Johnson, N. P. Impact of titanium adhesion layers on the response of arrays of metallic split-ring resonators (SRRs). *Opt. Express* **2010**, *18*, 11202–8.
- (29) Jiao, X. J.; Goeckeritz, J.; Blair, S.; Oldham, M. Localization of Near-Field Resonances in Bowtie Antennae: Influence of Adhesion Layers. *Plasmonics* **2009**, *4*, 37–50.
- (30) Sexton, B.A.F.; Feltis, B. N.; Davis, T. J. Characterisation of gold surface plasmon resonance sensor substrates. *Sens. Actuators, A* **2008**, *141*, 471–475.
- (31) Henager, C. H., Jr.; Pawlewicz, W. T. Thermal conductivities of thin, sputtered optical films. *Appl. Opt.* **1993**, *32*, 91–101.
- (32) Chen, G.; Hui, P. Thermal conductivities of evaporated gold films on silicon and glass. *Appl. Phys. Lett.* **1999**, *74*, 2942.
- (33) Fu, Y.; Zhang, J.; Lakowicz, J. R. Plasmon-Enhanced Fluorescence from Single Fluorophores End-Linked to Gold Nanorods. *J. Am. Chem. Soc.* **2010**, *132*, 5540–1.
- (34) Dondapati, S. K.; et al. Label-free Biosensing Based on Single Gold Nanostars as Plasmonic Transducers. *ACS Nano* **2010**, *4*, 6318–6322.
- (35) Ohlinger, A.; Deak, A.; Lutich, A. A.; Feldmann, J. Optically Trapped Gold Nanoparticle Enables Listening at the Microscale. *Phys. Rev. Lett.* **2012**, *108*, 018101.
- (36) Wienken, C. J.; Baaske, P.; Rothbauer, U.; Braun, D.; Duhr, S. Protein-binding assays in biological liquids using microscale thermophoresis. *Nat. Commun.* **2010**, *1*, 100.
- (37) Kyrsting, A.; Bendix, P. M.; Oddershede, L. B. Mapping 3D Focal Intensity Exposes the Stable Trapping Positions of Single Nanoparticles. *Nano Lett.* **2013**, *13*, 31–5.
- (38) Johnson, P. B.; Christy, R. W. Optical Constants of the Noble Metals. *Phys. Rev. B* **1972**, *6*, 4370–4379.
- (39) Lynch, D.; Olson, C.; Weaver, J. Optical properties of Ti, Zr, and Hf from 0.15 to 30 eV. *Phys. Rev. B* **1975**, *11*, 3617–3624.
- (40) Grundum, B. C.; Cahill, D. G.; Averback, R. S. Thermal conductance of metal-metal interfaces. *Phys. Rev. B* **2005**, *72*, 245426.
- (41) Käding, O. W.; Skurk, H.; Goodson, K. E. Thermal Conduction in Metallized Silicon-Dioxide Layers on Silicon. *Appl. Phys. Lett.* **1994**, *65*, 1629–1631.